Coulomb dissociation of ^{27}P at 500 MeV/u

J. Marganiec,[1,2,3,*] S. Beceiro Novo,[4,5] S. Typel,[2] C. Langer,[5,6,7] C. Wimmer,[7] H. Alvarez-Pol,[4] T. Aumann,[1,2] K. Boretzky,[2] E. Casarejos,[4,8] A. Chatillon,[2] D. Cortina-Gil,[4] U. Datta-Pramanik,[9] Z. Elekes,[10] Z. Fulop,[10] D. Galaviz,[11] H. Geissel,[2] S. Giron,[2] U. Greife,[12] F. Hammache,[13] M. Heil,[2] J. Hoffman,[2] H. Johansson,[14] O. Kiselev,[2] N. Kurz,[2] K. Larsson,[14] T. Le Bleis,[2,15] Yu. A. Litvinov,[2] K. Mahata,[2] C. Muentz,[7] C. Nociforo,[2] W. Ott,[2] S. Paschalis,[1,16] R. Plag,[2] W. Prokopowicz,[2] C. Rodríguez Tajes,[4] D. M. Rossi,[5,2,17] H. Simon,[2] M. Stanoiu,[2] J. Stroth,[7] K. Sümmerer,[2] A. Wagner,[18] F. Wamers,[1,2] H. Weick,[2] and M. Wiescher[19]

(R3B Collaboration)

[1]*Technische Universität Darmstadt, D-64289 Darmstadt, Germany*

[2]*GSI Helmholtzzentrum für Schwerionenforschung, D-64291 Darmstadt, Germany*

[3]*ExtreMe Matter Institute EMMI-GSI, D-64291 Darmstadt, Germany*

[4]*Universidade de Santiago de Compostela, E-15782 Santiago de Compostela, Spain*

[5]*National Superconducting Cyclotron Laboratory, Michigan State University, East Lansing, Michigan 48824-1321, USA*

[6]*Joint Institute for Nuclear Astrophysics—CEE, Michigan State University, East Lansing, Michigan 48824, USA*

[7]*Johann-Wolfgang-Goethe-Universität, D-60438 Frankfurt am Main, Germany*

[8]*University of Vigo, E-36310 Vigo, Spain*

[9]*SINP, Kolkata 700-064, India*

[10]*ATOMKI, P.O. Box 51, H-4001 Debrecen, Hungary*

[11]*CSIC, E-28006 Madrid, Spain*

[12]*Colorado School of Mines, Golden, Colorado 80401, USA*

[13]*IPN, UMR-8608, CNRS/IN2P3 and Universite Paris Sud XI, F-91406 Orsay, France*

[14]*Chalmers Institute of Technology, S-41296 Göteborg, Sweden*

[15]*Technische Universität München, D-80333 München, Germany*

[16]*University of Liverpool, Liverpool L69 7ZE, United Kingdom*

[17]*Johannes-Gutenberg-Universität, D-55128 Mainz, Germany*

[18]*Forschungszentrum Rossendorf, D-01314 Dresden, Germany*

[19]*JINA, University of Notre Dame, Notre Dame, Indiana 46556, USA*

(Received 11 March 2015; revised manuscript received 25 November 2015; published 26 April 2016)

The proton-capture reaction ^{26}Si(p,γ)^{27}P was studied via Coulomb dissociation (CD) of ^{27}P at an incident energy of about 500 MeV/u. The three lowest-lying resonances in ^{27}P have been populated and their resonance strengths have been measured. In addition, a nonresonant direct-capture component was clearly identified and its astrophysical S factor measured. The experimental results are compared to Monte Carlo simulations of the CD process using a semiclassical model. Our thermonuclear reaction rates show good agreement with the rates from a recent compilation. With respect to the nuclear structure of ^{27}P we have found evidence for a negative-parity intruder state at 2.88-MeV excitation energy.

DOI: 10.1103/PhysRevC.93.045811

I. INTRODUCTION

The observation of a 1.8-MeV γ transition in the galactic plane of the Milky Way by satellite-borne spectrometers like COMPTEL/CGRO [1] or SPI/INTEGRAL [2] was a breakthrough in the study of stellar nucleosynthesis. The observation of this transition, originating from the decay of the ^{26}Al isomeric 5^+ state (with a half-life of 0.72 My) to the first 2^+ state in ^{26}Mg, proves that nucleosynthesis of ^{26}Al is an ongoing process in our galaxy. The nuclear-reaction network around ^{26}Al can be viewed, e.g., in Fig. 3.1 of Ref. [3]. This network involves the very proton-rich nucleus ^{26}Si. In principle, the β decay of ^{26}Si does not give rise to the 1.8-MeV γ ray because it feeds the ^{26}Al isomeric 0^+ state which in turn decays quickly ($T_{1/2} = 6.3$ s) to the 0^+ ground state of ^{26}Mg. If, however, under sufficiently hot conditions, the isomeric ^{26}Al 0^+ state is in thermal equilibrium with the ^{26}Al 5^+ ground state, the amount of ^{26}Si produced in a stellar environment could play a role. For detailed reaction-network calculations, e.g., in nova or x-ray burst environments, it is therefore important to reliably calculate the destruction (via β decay or the (p,γ) reaction) of ^{26}Si in those environments. For this purpose, the reaction rate of the proton-capture reaction ^{26}Si(p,γ)^{27}P must be known.

Under nova conditions, the reaction flow through ^{26}Si(p,γ)^{27}P was investigated by Caggiano *et al.* [4] in their pioneering paper where the energies of the two lowest-lying resonances in ^{27}P were measured for the first time. They had, however, to rely on shell-model calculations to derive the resonance strengths of both of these resonances. The same holds for the most recent comprehensive rate evaluation by Iliadis *et al.* [5], which is the currently suggested rate in the REACLIB [6] and STARLIB [7] compilations. Both the direct-

*j.marganiec@gsi.de

capture S factor and the resonance strengths are either based on shell-model calculations or on mirror-level properties.

An experimental approach to measure the resonance strength is the time-reversed process, Coulomb dissociation (CD). By applying the concept of detailed balance, the CD cross section can be converted to a radiative-capture cross section and subsequently to a resonance strength. For the case of ^{27}P, a CD experiment was performed, at an incident energy of 54.2 A MeV, at the RIKEN laboratory by shooting a low-intensity radioactive ^{27}P beam onto a lead target [8]. In addition to the two lowest-lying resonances found by Caggiano *et al.* [4], two higher-lying resonances were found. Resonance strengths for the two $5/2^+$ levels at 1.67- and 2.23-MeV excitation energy could be measured. The resonance strength for the lowest $3/2^+$ state at 1.18 MeV (reached predominantly by $M1$ multipolarity in CD) could not be measured and had to be calculated relying on the $M1/E2$ mixing ratio of the corresponding γ transition in the mirror nucleus ^{27}Mg.

The present paper follows the approach of Togano *et al.* [8], but studies the CD of ^{27}P at the considerably higher incident energy of 500 A MeV. This allows higher luminosities through the use of thicker Pb breakup targets and a larger acceptance of the reaction products from stronger forward focusing of the fragment velocity vectors. Because we cannot distinguish experimentally between Coulomb and nuclear interactions of ^{27}P with the Pb target, we have used a low-Z ^{12}C target to quantify the nuclear interactions and, after a suitable scaling, subtract those solely nuclear-induced spectra from the total ones. This subtraction could not be performed in the work of Togano *et al.* [8]. Our higher incident energy causes also a harder spectrum of virtual photons inducing the CD process. This should allow one to detect a more pronounced direct-capture component which strongly increases with excitation energy.

We start this article in Sec. II by discussing what is known at present about the nuclear structure of ^{27}P and how this can be modeled theoretically with a simple potential model. This is followed by a semiclassical description of the CD process. In Sec. III we describe the experimental setup used to detect the breakup particles and coincident γ rays in complete kinematics.

Section IV is devoted to a comprehensive description of the data analysis and the experimental results. A discussion of our results is given in Sec. V, and is followed by a detailed extraction of the astrophysical reaction rate and a comparison to previously derived rates in the final Sec. VI.

II. THEORETICAL CONSIDERATIONS

A. Nuclear structure of ^{27}P

Despite the fact that the nucleus ^{27}P is located only one neutron away from the proton-drip line, some features of its low-lying level structure are known (Fig. 1). Its ground-state mass excess and the location of the first two resonances above the one-proton separation energy of 870(26) keV [9] have been found by Caggiano *et al.* using the ^{28}Si(^{7}Li,^{8}He)^{27}P reaction [4]. Resonances at 1199(19) keV ($3/2^+$) and 1615(21) keV ($5/2^+$) excitation energy were identified; spin-parity assignments were derived from known states in the mirror nucleus ^{27}Mg [10]. Later, Gade *et al.* [11] confirmed the existence of the $3/2^+$ resonance, located at 1120(8) keV, using proton knockout from a ^{28}Si beam. This experiment provided also a spectroscopic factor for the $d_{3/2}$ shell-model configuration of this resonance.

The CD experiment by Togano *et al.* [8] found levels at 1176(32) and 1666(42) keV, thus confirming the prior results; in addition, another resonance at 2230(100)-keV and a tentative one at 3060(90)-keV excitation energy were identified. From both, shell-model and mirror-nucleus systematics, the 2.23-MeV level can be identified with the second $5/2^+$ resonance.

Several resonances above 2.8-MeV excitation energy were identified in a ^{26}Si+p elastic-scattering experiment [12]. By applying an R-matrix analysis, Jung *et al.* could derive spin-parity assignments of several levels between 2.88- and 3.60-MeV excitation energy. These levels are interesting from a nuclear-structure point of view, but are too far away from the proton binding energy to be relevant in astrophysical scenarios.

B. Potential-model description of ^{27}P

To calculate the cross section of the radiative proton capture on ^{26}Si and that of the Coulomb dissociation of ^{27}P we developed a simple two-particle potential model that can describe the main features relevant for the two types of reactions. An approach with a valence proton + ^{26}Si core picture is sufficient because the proton separation energy S_p of the ^{27}P ground state is small and the excited states in the continuum are usually well described as single-particle resonances. All reaction calculations are performed with the help of the program CDXS+ [13].

Because the $1/2^+$ ground state of the nucleus ^{27}P is deformed, the orbital angular momentum ℓ is not a good quantum number of the wave function for the relative motion between the proton and the core. From a Skyrme-Hartree Fock (SHF) calculation, which was designed for the description of

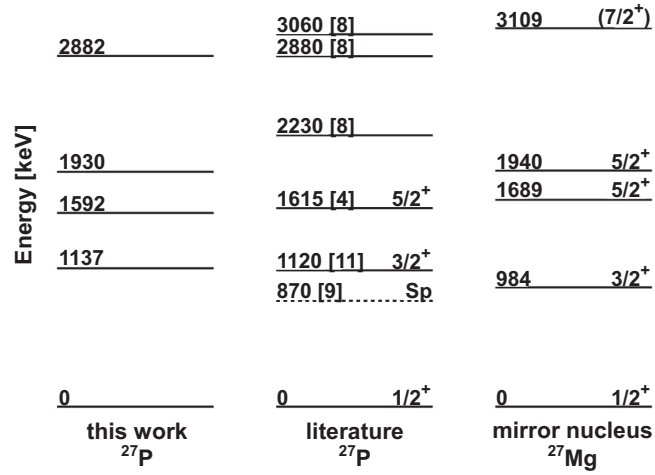

FIG. 1. Levels in ^{27}P from the present and other experiments [4,8,11,12] in comparison with those of the mirror nucleus ^{27}Mg [10]. The proton-separation energy S_p was taken from Ref. [9].

TABLE I. Parameters for the scattering states in the single-particle model and multipolarities for the excitation from the ^{27}P ground state. See text for notation.

J^π	E_r (MeV)	$\Pi\lambda$	ℓ_j	$J_c^{\pi_c}$	$V_{\ell_j}^{J^\pi J_c}$ (MeV)
$\frac{1}{2}^+$	–	$M1, E2$	$s_{1/2}$	0^+	46.48040
			$d_{3/2}$	2^+	45.875047
			$d_{5/2}$	2^+	45.875047
$\frac{1}{2}^-$	–	$E1$	$p_{1/2}$	0^+	75.86
			$p_{3/2}$	0^+	75.86
			$p_{3/2}$	2^+	75.86
			$f_{5/2}$	2^+	75.86
$\frac{3}{2}^+_1$	0.267	$M1, E2$	$d_{3/2}$	0^+	43.760952
			$s_{1/2}$	2^+	43.834218
			$d_{3/2}$	2^+	43.760952
			$d_{5/2}$	2^+	43.760952
$\frac{3}{2}^+_2$	2.012	$M1, E2$	$d_{3/2}$	0^+	40.21013
			$s_{1/2}$	2^+	38.23463
			$d_{3/2}$	2^+	40.21013
			$d_{5/2}$	2^+	40.21013
$\frac{3}{2}^+$	–	$E2$	$g_{7/2}$	2^+	75.86
$\frac{3}{2}^-$	–	$E1$	$p_{1/2}$	2^+	75.86
			$p_{3/2}$	2^+	75.86
			$f_{5/2}$	2^+	75.86
$\frac{3}{2}^-$	2.012	$E1$	$f_{7/2}$	2^+	63.77176
$\frac{5}{2}^+_1$	0.722	$E2$	$d_{5/2}$	0^+	42.8801747
			$s_{1/2}$	2^+	42.641388
			$d_{3/2}$	2^+	42.8801747
			$d_{5/2}$	2^+	42.8801747
$\frac{5}{2}^+_2$	1.060	$E2$	$d_{5/2}$	0^+	42.208818
			$s_{1/2}$	2^+	41.654775
			$d_{3/2}$	2^+	42.208818
			$d_{5/2}$	2^+	42.208818
$\frac{5}{2}^+_3$	2.012	$E2$	$d_{5/2}$	0^+	40.21013
			$s_{1/2}$	2^+	38.23463
			$d_{3/2}$	2^+	40.21013
			$d_{5/2}$	2^+	40.21013
$\frac{5}{2}^+$	–	$E2$	$g_{7/2}$	2^+	75.86
			$g_{9/2}$	2^+	75.86

deformed axially symmetric nuclei [14], using the SKX interaction [15], it is found that ^{27}P is prolate with a deformation parameter of $\beta_2 = 0.247$. The major components of the wave function are s-wave and d-wave proton single-particle states that can couple to $J_c^{\pi_c} = 0^+$ and 2^+ core states to reproduce the ground-state spin and parity of ^{27}P. Thus the ground-state wave function is written in a jj coupling scheme as

$$
\begin{aligned}
|\Psi_{gs}(^{27}\mathrm{P})\rangle = {} & A_{s_{1/2}} \big|\big[\phi_{s_{1/2}}(p) \otimes \Phi_{0^+}(^{26}\mathrm{Si})\big]_{J^\pi=\frac{1}{2}^+}\big\rangle \\
& + A_{d_{3/2}} \big|\big[\phi_{d_{3/2}}(p) \otimes \Phi_{2^+}(^{26}\mathrm{Si})\big]_{J^\pi=\frac{1}{2}^+}\big\rangle \\
& + A_{d_{5/2}} \big|\big[\phi_{d_{5/2}}(p) \otimes \Phi_{2^+}(^{26}\mathrm{Si})\big]_{J^\pi=\frac{1}{2}^+}\big\rangle, \quad (1)
\end{aligned}
$$

with amplitudes $A_{s_{1/2}} = 0.82037, A_{d_{3/2}} = 0.45166$, and $A_{d_{5/2}} = 0.35071$ obtained from the SHF model. $S_{\ell_j} = |A_{\ell_j}|^2$ represent the corresponding spectroscopic factors of the three configurations. Instead of using the original SHF single-particle wave functions $\phi_{l_j}(p)$ in the subsequent calculations, we take them as solutions (with the appropriate number of nodes) of a Schrödinger equation containing a central potential of the Woods-Saxon form with radius parameter $r_0 = 1.25$ fm and diffuseness parameter $a = 0.65$ fm. The depths V_ℓ of the central potentials are adjusted to reproduce the correct breakup threshold energy $E_{\mathrm{thr}} = 0.87$ MeV. We find $V_s = 46.48040$ MeV and $V_d = 45.875047$ MeV for the $\ell = 0$ and $\ell = 2$ partial waves, respectively. The many-body wave functions $\Phi_{0^+}(^{26}\mathrm{Si})$ and $\Phi_{2^+}(^{26}\mathrm{Si})$ are assumed as inert states of the core nucleus. Note that these two states do not correspond to the ground and first excited state of ^{26}Si but represent the deformed ground state of the core.

The Coulomb dissociation of ^{27}P proceeds predominantly through $\Pi\lambda = E1, M1$, and $E2$ transitions from the initial state (1) to p+^{26}Si scattering states in the continuum. The selection rules for these transitions determine the spins and parities of the relevant final states. They are $J^\pi = 1/2^-$, $3/2^-$ for $E1$ excitations, $1/2^+$,$3/2^+$ for $M1$ excitations, and $3/2^+$,$5/2^+$ for $E2$ excitations. Thus only a limited number of resonances can be reached. For example, a breakup through channels with $J^\pi = 7/2^+$ is not expected to occur in Coulomb dissociation. In analogy to Eq. (1), the final state wave functions are written as

$$
\begin{aligned}
& \big|\Psi_{sc}^{J^\pi}(^{27}\mathrm{P})\big\rangle \\
& \quad = \sum_{\ell_j, J_c} B_{\ell_j}^{J^\pi J_c} \big|\big[\psi_{\ell_j}^{J^\pi J_c}(p) \otimes \Phi_{J_c^{\pi_c}}(^{26}\mathrm{Si})\big]_{J^\pi}\big\rangle, \quad (2)
\end{aligned}
$$

with proton single-particle scattering wave functions $\psi_{\ell_j}^{J^\pi J_c}$ that are obtained from solving the Schrödinger equation of the p-core relative motion for energies E in the continuum with Woods-Saxon-type central potentials of the same shape as for the ground-state wave function. The depths $V_{\ell_j}^{J^\pi J_c}$ in the channels with resonances are adjusted to reproduce the corresponding excitation energies $E_{\mathrm{exc}} = E_r + E_{\mathrm{thr}}$. The resonance energies E_r were taken from the analysis of the present breakup experiment; see below. The actual values of the resonance energies and potential depths are given in Table I. In the case of the resonance at $E_r = 2.012$ MeV, three different possibilities for the total angular momentum and parity were considered: (a) a second $3/2^+$ state, (b) a third $5/2^+$ state, and (c) a $3/2^-$ intruder state with orbital angular momentum $\ell = 3$. In the latter case there is no contribution of channels with a 0^+ core state. A $3/2^-$ state can be excited strongly by an $E1$ transition from the ^{27}P ground state but negative-parity states are not considered in shell-model calculations for sd-shell nuclei. However, such an intruder state can be expected from the trend of negative-parity states in the neighboring odd-A isobar chains. For $A = 27$ isobars the situation is unclear [10], but for $A = 25$ [16] and $A = 29$ [17] isobars, a shift of negative-parity states to lower excitation energies as compared to positive-parity states is observed when the nuclei become

TABLE II. Resonance parameters of ^{27}P in the present potential model and other theoretical and experimental work.

J^π	Reference	E_r (MeV)	Γ_p (eV)	Multipolarity $\Pi\lambda$	Γ_γ (eV)	Γ (eV)	$\omega\gamma$ (eV)
$\frac{3}{2}^+_1$	This work	0.267	5.229×10^{-4}	$M1$	8.078×10^{-4}	1.331×10^{-3}	6.349×10^{-4}
	this work	0.267	5.229×10^{-4}	$E2$	2.060×10^{-5}	5.436×10^{-4}	3.965×10^{-5}
	this work	0.267	5.229×10^{-4}	$M1$+$E2$	9.499×10^{-4}	1.473×10^{-3}	6.745×10^{-4}
	[8]	0.315(17)	4.04×10^{-3}	$M1$	1.2×10^{-3}		$1.8(+1.9/-1.1) \times 10^{-3}$
	[8]	0.315(17)	4.04×10^{-3}	$E2$	9.6×10^{-5}		$6.5(13) \times 10^{-5}$
	[8]	0.315(17)	4.04×10^{-3}	$M1$+$E2$			$1.9(+1.9/-1.1) \times 10^{-3}$
	[22]	0.32	1.7×10^{-3}	$M1$+$E2$	1.36×10^{-3}		1.51×10^{-3}
	[4]	0.340(33)	3.5×10^{-3}	$M1$+$E2$	3.43×10^{-3}		3.5×10^{-3}
	[5]	0.259(28)	1.8×10^{-4}	$E2$	3.4×10^{-3}		
$\frac{5}{2}^+_1$	This work	0.722	$2.185 \times 10^{+1}$	$E2$	1.168×10^{-4}	$2.185 \times 10^{+1}$	3.504×10^{-4}
	[8]	0.805(32)		$E2$			$6.0(11) \times 10^{-4}$
	[22]	0.80	$1.361 \times 10^{+1}$	$E2$	3.3×10^{-4}		9.9×10^{-4}
	[4]	0.772	7.5	$E2$	3.30×10^{-4}		9.9×10^{-4}
	[5]	0.772(33)	4.3	$E2$	3.3×10^{-4}		
$\frac{5}{2}^+_2$	This work	1.060	$4.229 \times 10^{+2}$	$E2$	3.285×10^{-4}	$4.229 \times 10^{+2}$	9.854×10^{-4}
	[8]	1.37(10)		$E2$			$1.10(27) \times 10^{-3}$
	[5]	1.09(10)	4.4	$E2$	6.0×10^{-4}		
$\frac{3}{2}^+_2$	This work	2.012	$2.110 \times 10^{+4}$	$M1$	5.000×10^{-3}	$2.110 \times 10^{+4}$	1.000×10^{-2}
	This work	2.012	$2.110 \times 10^{+4}$	$E2$	3.015×10^{-3}	$2.110 \times 10^{+4}$	6.030×10^{-3}
	This work	2.012	$2.110 \times 10^{+4}$	$M1$+$E2$	8.015×10^{-3}	$2.110 \times 10^{+4}$	1.603×10^{-2}
$\frac{5}{2}^+_3$	This work	2.012	$2.130 \times 10^{+4}$	$E2$	3.055×10^{-3}	$2.130 \times 10^{+4}$	9.132×10^{-3}
$\frac{3}{2}^-$	This work	2.012	$1.603 \times 10^{+3}$	$E1$	1.143×10^{-1}	$1.603 \times 10^{+3}$	2.286×10^{-1}

more proton rich. In addition, the splitting of the $f_{7/2}$ state in a spherical nucleus into $J = 1/2^-, 3/2^-, 5/2^-$, and $7/2^-$ levels for a prolate nucleus as predicted by the Nilsson model [18] suggests a lowering of the $3/2^-$ level.

A different strategy was used to determine the potential depths in channels without resonance. For the $1/2^+$ contributions, the values are identical to those in the ^{27}P ground state. Because there is no information available for other nonresonant states in the continuum, the depth of the potentials in these channels with $\ell = 1, \ell = 3$, and $\ell = 4$ is chosen such that the continuum contribution to the Coulomb breakup cross section for energies $3\text{MeV} \leqslant E \leqslant 5\text{MeV}$ is reproduced. The coefficients $B_{\ell_j}^{J^\pi J_c}$ introduced in Eq. (2) are set to one as usual for proper scattering wave functions. Only in the case of the $3/2^-$ intruder state, a value smaller than one was considered in the analysis of the Coulomb breakup experiment to fit to the observed strength of the resonance and to compensate for the deficiencies of the simple model description.

C. Radiative-capture reaction

The matrix elements,

$$M_{\Pi\lambda}(J^\pi) = \left\langle \Psi_{sc}^{J^\pi}(^{27}\text{P}) \middle| \mathcal{M}(\Pi\lambda) | \Psi_{gs}(^{27}\text{P}) \right\rangle, \tag{3}$$

for the electromagnetic transitions from the ground state to the scattering states J^π in the ^{27}P system are calculated with the appropriate multipole transition operators $\mathcal{M}(\Pi\lambda)$. They contain standard effective charges $Z_{\text{eff}}^{(\lambda)} = Z_p[m_{\text{Si}}/(m_{\text{Si}} + m_p)]^\lambda + Z_{\text{Si}}[-m_p/(m_{\text{Si}} + m_p)]^\lambda$ for Eλ transitions. For the $M1$ transition, the experimental value of the proton magnetic dipole moment $2.793\mu_N$ is used in the calculation. From the matrix elements (3) the reduced transition probabilities $dB[\Pi\lambda, ^{27}\text{P}(1/2^+) \rightarrow p + ^{26}\text{Si}(J^\pi)]/dE$, the photoabsorption cross sections $\sigma_{\text{abs}}^{(\Pi\lambda)}(E)$ and finally, with the help of the theorem of detailed balance for inverse reactions, the cross sections for radiative capture $\sigma_{\text{cap}}^{(\Pi\lambda)}(E)$ for energies $E = E_{\text{exc}} - E_{\text{thr}} > 0$ are obtained. For narrow resonances, the radiative-capture cross section can be well described by a Breit-Wigner parametrization,

$$\sigma_{\text{cap}}(E) = \frac{\pi}{k^2}\omega\gamma \frac{\Gamma}{(E - E_r)^2 + \Gamma^2/4}, \tag{4}$$

with resonance energy E_r and total width $\Gamma = \Gamma_p + \Gamma_\gamma$ that is the sum of the proton width Γ_p and the much smaller γ width Γ_γ. The resonance strength,

$$\omega\gamma = \frac{2J + 1}{(2J_p + 1)(2J_{\text{Si}} + 1)} \frac{\Gamma_\gamma \Gamma_p}{\Gamma}, \tag{5}$$

depends on the widths and the total angular momenta of the resonance J, that of the proton J_p, and that of the core nucleus J_{Si}. The quantity $\hbar k = \sqrt{2\mu_{p\text{Si}}E}$ denotes the relative momentum in the p+^{26}Si system with reduced mass $\mu_{p\text{Si}} = m_p m_{\text{Si}}/(m_p + m_{\text{Si}})$. The resonance parameters in the present single-particle model are given in Table II. For the state at resonance energy $E_r = 2.012$ MeV the results for three possible choices for the spin and parity are given. Note that the γ widths Γ_γ and proton widths Γ_p of the low-energy $3/2^+$ resonance are of similar magnitude whereas $\Gamma_\gamma \ll \Gamma_p$ for all other states. The $E2/M1$ ratio for the lowest resonance is 0.0624 in the present potential model. This value is about 30%

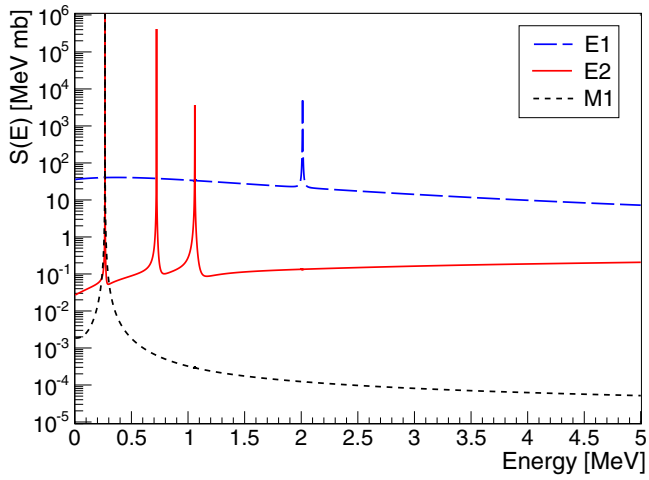

FIG. 2. Multipole contributions to the astrophysical S factor of the radiative-capture reaction ^{26}Si(p,γ)^{27}P.

larger than the experimental value of 0.0481 ± 0.0240 [19] and the theoretical value of 0.0458 in a shell-model calculation of the same transition of the mirror nucleus ^{27}Mg [20]. In Ref. [21] the smaller value of 0.033 is estimated from a simple single-particle model.

The radiative capture cross section of the ^{26}Si(p,γ)^{27}P reaction is easily converted to the astrophysical S factor,

$$S(E) = E\sigma_{\rm cap}(E)\exp(2\pi\eta), \tag{6}$$

with the Sommerfeld parameter $\eta = Z_p Z_{Si} e^2/(\hbar v)$ depending on the relative velocity $v = \hbar k/\mu_{\rm pSi}$. In Fig. 2 the dependence of the $E1, E2$, and $M1$ contributions to the S factor on the energy E is depicted assuming a $3/2^-$ spin and parity of the fourth resonance with $B^{J^\pi J_c}_{\ell_j} = 1$. The resonances show up as prominent spikes because of the very small widths. Note that the peak of the lowest resonance is outside of the figure with maxima of 6.05×10^{13} and 9.68×10^{14} MeV mb for the $E2$ and $M1$ contributions, respectively. The nonresonant direct capture to the ^{27}P ground state is dominated by $E1$ transitions from p waves leading to an almost constant contribution to the S factor. The zero-energy S factor is given in the potential model by $S(0) = 35.9$ keV b. This is similar to the theoretical result of $S(0) = 36.3$ keV b in Ref. [22]. In contrast, a much larger value of 87(11) keV b was obtained in Ref. [21] from the asymptotic normalization constant (ANC) of ^{27}Mg → ^{26}Mg + p assuming charge symmetry of mirror nuclei. Note that the zero-energy S factor derived in the ANC method usually assumes plane waves without interactions in the scattering states.

D. Coulomb dissociation of ^{27}P

The electromagnetic transition matrix elements of the potential model are used in the calculation of the cross section of the ^{208}Pb(^{27}P,^{26}Si p γ)^{208}Pb Coulomb-breakup reaction with beam energy of 491.3 MeV per nucleon. The differential breakup cross section,

$$\frac{d^3\sigma_{\rm CD}}{d\Omega_{\rm P-Pb} dE_{\rm p-Si} d\Omega_{\rm p-Si}} = \frac{\mu^2_{\rm P-Pb}}{(2\pi)^2\hbar^4}\frac{p^f_{\rm P-Pb}}{p^i_{\rm P-Pb}}\frac{\mu_{\rm p-Si}p_{\rm p-Si}}{(2\pi)^3} \sum_{\rm LM} A_{\rm LM} Y_{\rm LM}(\hat{p}_{\rm p-Si}), \tag{7}$$

with reduced masses and relative momenta of the various particle combinations takes the dependence on the ^{27}P-^{208}Pb scattering angle and the relative momentum in the p-^{26}Si system fully into account including interference effects of the various electromagnetic multipole contributions. The complex coefficients $A_{\rm LM}(\Omega_{\rm P-Pb}, E_{\rm p-Si})$ depend on the transition matrix elements [Eq. (3)] and Coulomb excitation functions that are calculated in the semiclassical relativistic approximation [23]. After integration over ^{27}P-^{208}Pb scattering angles up to the grazing angle of ≈1.5° and over all p-^{26}Si relative momentum directions, the energy-dependent ($E = E_{\rm p-Si}$) single differential breakup cross section results in

$$\frac{d\sigma_{\rm CD}}{dE} = \int d\Omega_{\rm P-Pb}\int d\Omega_{\rm p-Si}\frac{d^3\sigma}{d\Omega_{\rm P-Pb}dE_{\rm p-Si}d\Omega_{\rm p-Si}} = \frac{1}{E_\gamma}\sum_{\Pi\lambda}\sigma^{\Pi\lambda}_{\rm abs}(E) n_{\Pi\Lambda}, \tag{8}$$

with the photoabsorption cross sections $\sigma^{\Pi\lambda}_{\rm abs}(E)$ and virtual photon numbers $n_{\Pi\Lambda}$. Because the multipoles do not interfere in Eq. (8), the individual contributions to the cross section can be depicted separately as shown in Fig. 3. Because of the abundant number of $E2$ virtual photons in Coulomb excitation, the $E1$-to-$E2$ ratio is much smaller than in the S factor. Also, the $M1$ breakup contribution is considerably reduced relative to the $E2$ component. Thus the Coulomb dissociation will be mostly sensitive to the $E2$ transitions and the $E1$ excitation to the continuum is expected to show up only at higher excitation energies in the experiment. The strong suppression of the breakup cross section at low excitation energies is clearly visible, it is caused by the strong Coulomb repulsion between

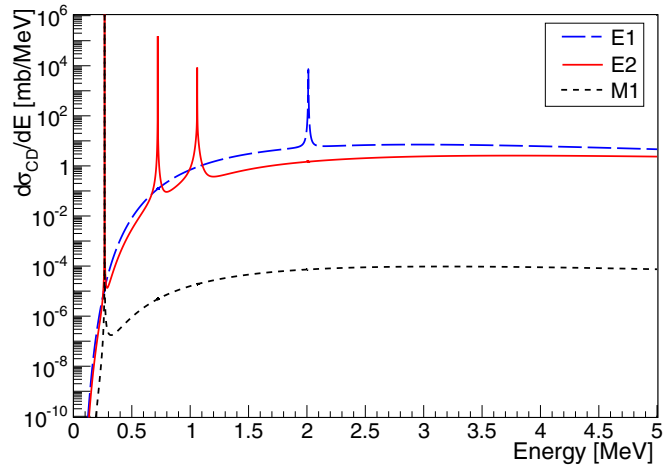

FIG. 3. Multipole contributions to the differential cross section of the breakup reaction ^{208}Pb(^{27}P,^{26}Si p γ)^{208}Pb at 491.3A MeV incident beam energy.

TABLE III. Cross sections for the Coulomb excitation of ^{27}P at 491.3A MeV populating individual resonances in the present potential model.

E_r (MeV)	$E_{\rm exc}$ (MeV)	Transition	$\sigma_{\rm CD}$ (mb)
0.267(20)	1.137	$\frac{1}{2}^+_{gs} \rightarrow \frac{3}{2}^+_1$	3.76
0.722(56)	1.592	$\frac{1}{2}^+_{gs} \rightarrow \frac{5}{2}^+_1$	5.64
1.060(170)	1.930	$\frac{1}{2}^+_{gs} \rightarrow \frac{5}{2}^+_2$	6.05
2.012(76)	2.882	$\frac{1}{2}^+_{gs} \rightarrow \frac{3}{2}^+_2$	5.19
2.012(76)	2.882	$\frac{1}{2}^+_{gs} \rightarrow \frac{5}{2}^+_3$	7.81
2.012(76)	2.882	$\frac{1}{2}^+_{gs} \rightarrow \frac{3}{2}^-$	17.95

the proton and ^{26}Si. The theoretical cross sections for the Coulomb excitation of the various resonances are given in Table III.

The full triple differential cross section [Eq. (7)] is used to generate a distribution of breakup events by a Monte Carlo simulation in the ^{27}P rest system. Using relativistic kinematics the four-momenta of the two breakup fragments, p and ^{26}Si, in the laboratory system are determined. They characterize uniquely each breakup event. The theoretical event distribution can be analyzed subsequently in the same way as experimental data.

III. EXPERIMENTAL PROCEDURES

To measure the CD of ^{27}P in complete kinematics, an experiment was performed at the GSI Helmholtzzentrum für Schwerionenforschung in Darmstadt, Germany. A schematic view of the LAND-R^{3}B setup used for the measurement is shown in Fig. 4. The setup is similar to the description in [24], however, a detailed explanation of the individual detectors is outlined in the next sections. The setup comprises several detectors allowing the identification and reconstruction of the four-momentum of each individual particle on an event-by-event basis.

A. Preparation of the ^{27}P secondary beam

The ^{27}P secondary beam was produced by fragmenting a 615.5 A MeV ^{36}Ar primary beam impinging on a 4.19-g/cm^2 ^{9}Be target.

The ^{27}P beam ($t_{1/2} = 260$ ms) was separated in flight in the two-stage fragment-separator FRS [25] by the $B\rho - \Delta E - B\rho$ technique. The ^{27}P ions reached the achromatic end focus F_8 of the FRS with an energy of 491.3 A MeV. Because of the finite momentum acceptance of the FRS some contaminants with similar $B\rho$ were also delivered to the experimental station. These cocktail-beam species could, however, uniquely be identified by means of their positions and times of flight measured in two plastic scintillators located at the dispersive midfocus of FRS F_2, and at F_8. In addition, position, time-of-flight, and energy loss were also measured in front of the secondary reaction target of the experimental setup by scintillators and position-sensitive pin diodes (PSP); see Fig. 4. The (x, y) measurements in the two PSP allowed one to define the reaction vertex at the target.

The mixed beam was directed onto a secondary target station located at the center of a 4π NaI array (Crystal Ball, XB). A 515-mg/cm^2 $^{\rm nat}$Pb target was used to induce electromagnetic excitations allowing one to study the CD of ^{27}P. The measurement included also several runs with a 660-mg/cm^2 ^{12}C target to study the nuclear-induced breakup. Reactions in different sections of the beam line other than the target were eliminated by subtracting properly scaled data files taken without target.

B. Detection of ^{26}Si breakup fragments

After the secondary reaction target, a double-sided Si microstrip detector (DSSSD) was placed to measure the position (x, y) and energy loss of the reaction products of the CD of ^{27}P, ^{26}Si, and proton. To separate both breakup fragments and measure their momenta, a large-area dipole magnet (ALADIN) was used. Its magnetic field was chosen to bend the ^{26}Si fragments by 16.7 degrees and the protons by 31 degrees.

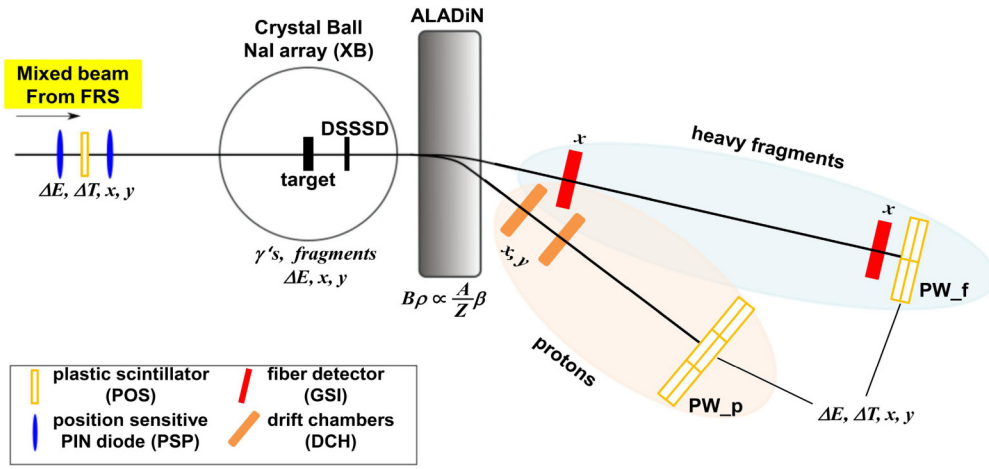

FIG. 4. Schematic view of the experimental setup used to detect CD of ^{27}P in complete kinematics. The physical quantities measured with the various detectors are indicated. Some technical details for the detectors are given in the text. The figure is adapted from Ref. [24].

Tracking of ^{26}Si was performed by two large-area scintillating-fiber detectors (GFI) [26,27]. The GFI provide horizontal position measurements (x) of fragments with high precision. They cover an area of almost 50×50 cm^2 and consist of 475 thin and long ($0.1 \times 50 \times 0.1$ cm^3) scintillator fibers coupled to position-sensitive photomultiplier (PM) tubes.

A dedicated tracking algorithm was developed, which accurately reconstructs the trajectory of each particle from the hit positions measured in the DSSSD in front of and in the two GFI behind ALADIN, resulting in a precise four-momentum measurement for each fragment (see Sec. IV B).

Behind the GFI, a plastic-scintillator wall (PW_f) provided time, position, and energy-loss measurements of the different heavy fragments. The wall consists of eight paddles ($6 \times 50 \times 0.5$ cm^3) in horizontal and eight identical paddles in vertical direction, thus covering roughly 48×48 cm^2 of active area. All paddles are read out on both sides by PM tubes. Hits in PW_f were used for triggering.

C. Detection of breakup protons

Two multiwire drift chambers (DCH) were installed to measure the positions of breakup protons behind ALADIN. Each DCH covers an active area of 100×80 cm^2. It consists of an x and a y plane placed in a common housing. For each plane, six layers of field wires define two layers of hexagonal drift cells. Each individual drift cell has a diameter of $\approx$16 mm and is read out via one sense wire in its center. There are 144 sense wires for detection in the x and 112 in the y direction, adding up to 256 readout channels for each DCH. The geometry and the operational parameters were optimized to detect minimum-ionizing particles with an efficiency larger than 95% and a spatial resolution better than 0.2 mm.

Behind the DCH, protons were registered in a large-area plastic-scintillator wall (PW_p) used also for triggering purposes. The wall consists of 18 paddles ($10 \times 147 \times 0.5$ cm^3) mounted vertically and 14 paddles ($189 \times 10 \times 0.5$ cm^3) mounted horizontally. All paddles are read out on both sides by PM tubes.

A similar tracking algorithm as the one used for the heavy fragments was optimized to calculate the four-momenta of the protons by reconstructing their trajectory from the vertex position in the target and the two hits measured in the DCH (see Sec. IV B). The intrinsic momentum resolution was estimated to be $\Delta p/p = 3 \times 10^{-3}$ with the help of Monte Carlo simulations.

D. Detection of coincident γ rays

Around the target a spherical 4π γ-ray detector (Crystal Ball, XB [28]) was mounted to detect coincident γ rays from the de-excitation of the reaction fragments. XB consists of 162 NaI(Tl) crystals, read out by PM tubes, forming a sphere with a 25-cm inner radius. Each crystal covers the same solid angle of 77 msr and has a thickness of 20 cm. The relatively high granularity of XB allows for the correction of the Doppler shift and broadening caused by the high velocities of the beam. An add-back algorithm was developed to recover the total energy of γ rays Compton scattered from one crystal to another.

IV. DATA ANALYSIS AND RESULTS

A. Incident ^{27}P projectiles

To identify the incoming ions, the determination of their nuclear charges and masses is needed. The ratio A/Z of a fully stripped ion passing through a constant magnetic field B can be expressed by

$$A/Z = \frac{e}{uc}\frac{B\rho}{\beta\gamma}, \tag{9}$$

where e is the charge of the electron, u the atomic mass unit, c the speed of light, and β and γ the usual relativistic velocity parameters. The determination of A/Z of an ion requires one to measure its velocity β, and its magnetic rigidity ($B\rho$). The velocity is obtained through a time-of-flight measurement from the FRS focus F_8 to the POS detector and the known flight path, provided by the positioning of the detectors; see Sec. III A. The magnetic rigidity ($B\rho$) is obtained by correcting the nominal rigidity $(B\rho)_0$ of an ion traveling on the central trajectory of the FRS by measured position deviations at the dispersive midfocus of FRS, F_2, and the achromatic end focus F_8. $(B\rho)_0$ is given by the actual magnet setting B, and the nominal radius of the central trajectory ρ_0.

With the measured velocity and magnetic rigidity of the ion, the mass-over-charge ratio is obtained [Eq. (9)]. The charge of each ion Z is calculated from the energy-loss measured in the PSP (Fig. 4). Absolute calibrations of all detectors used were performed by utilizing energy-loss and time-of-flight measurements with primary beams at known energies in combination with the ATIMA package for calibration of the energy loss in the detector material [29,30]. The resulting identification plot of the secondary beam impinging on the secondary reaction target is shown in Fig. 5.

To focus on reactions with ^{27}P only, a two-dimensional gate was used to select the desired isotope in the incoming channel (dashed contour in Fig. 5).

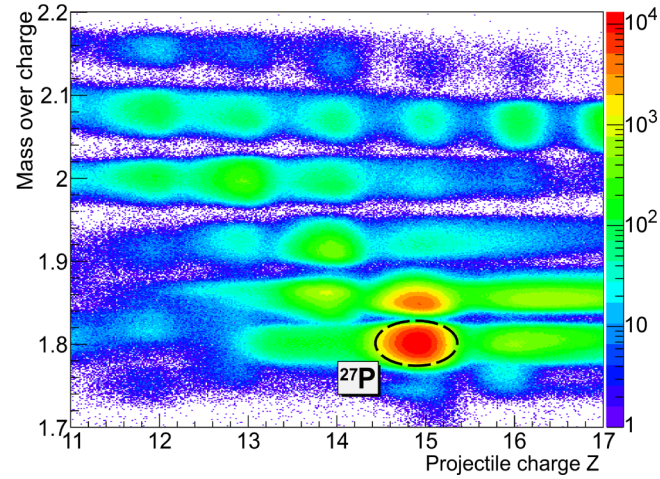

FIG. 5. Particle-identification plot of the secondary beam from the FRS as derived from magnetic-rigidity, time-of-flight, and energy-loss measurements. The two-dimensional gate used to select ^{27}P is indicated by the dashed contour line. The color scale is logarithmic.

B. Tracking procedure

An important part of the analysis is the tracking procedure of the outgoing ^{26}S fragments and protons behind the target. The aim of this procedure is to combine single hits in individual detectors to one physically meaningful particle trajectory with a certain mass, charge, and momentum. To determine the four-momentum of each particle, the tracking algorithm matches theoretically calculated trajectories with the measured ones in an iterative procedure. First the tracker algorithm determines positions and entrance angles before the ALADIN magnet and calculates the theoretical trajectory, starting with reasonable guess values for the momentum. From this theoretical trajectory, hit positions in the detectors are calculated and compared to the measured ones. The tracking algorithm then repeats the procedure [31] with improved momentum values until the deviations between measured and calculated hits become minimal. In reality, the tracking algorithm used works in "backward mode," starting from the last detector and tracking towards the target. Tracking in the heavy-fragment branch is calibrated using the well-known unreacted beam of ^{27}P [32]. This tracking algorithm was successfully used in other experiments [31,33].

C. Outgoing ^{26}Si and proton ejectiles

To identify the CD reaction channel (^{26}Si + proton), coincidences between a ^{26}Si ion in the heavy-fragment arm and a proton in the proton arm behind the ALADIN magnet (see Fig. 4) have to be selected. Figure 6 shows the identification of different heavy fragments via energy-loss measurements directly behind the target in the DSSSD and in the scintillator wall PW_f at the end of the setup. Several reaction products can be clearly identified. A two-dimensional gate was used to select the nuclei with $Z = 14$ (Si).

In combination with the tracking algorithm (see Sec. IV B), the mass of each Si ion was inferred (Fig. 7). The mass resolution in this case is 1.1%. In Fig. 7 it is noticeable that

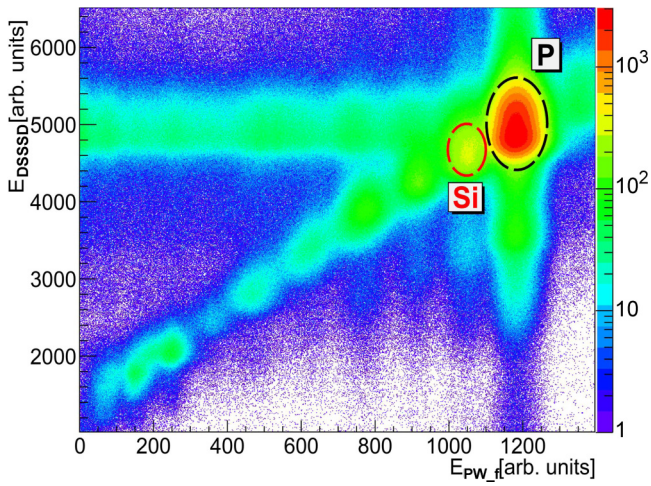

FIG. 6. Energy loss measured in the two-layer double-sided Si microstrip detector (DSSSD) behind the Pb target plotted versus the energy loss in the plastic-scintillator wall (PW_f). The color scale is logarithmic.

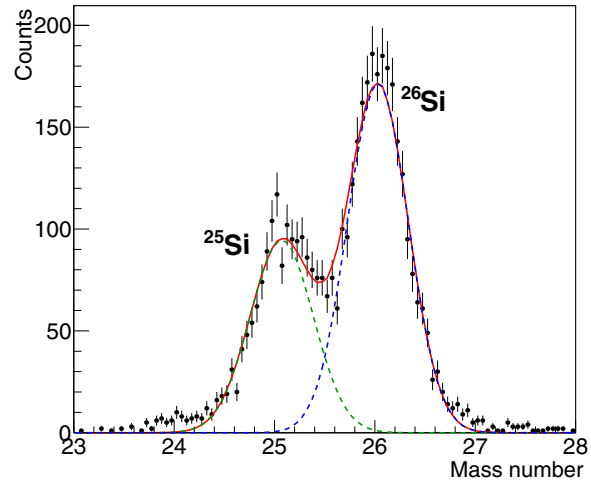

FIG. 7. Mass distribution of Si fragments detected behind the Pb breakup target. Events have been selected with gates on ^{27}P in front of and on $Z = 14$ (Si) behind the target, in coincidence with a proton in the proton arm.

the peak of ^{26}Si overlaps with the peak of ^{25}Si. However, the contamination of ^{25}Si in the ^{26}Si peak is negligible (3.6%) if we cut at mass number 25.5.

To select a breakup proton, the tracker requires that hits in both DCH detectors and in PW_p lie on a straight line. This helps to distinguish the "good" protons stemming from reactions in the target from the "bad" ones created in windows, detector frames, air, and other layers of matter. As Fig. 8 shows, the "good" protons show nicely correlated x and y positions in both DCH detectors; only few events are found off the diagonal.

Using these position measurements, the tracker algorithm (see Sec. IV B) provided four-momenta of the protons. The average intrinsic efficiency of the DCH was determined by analyzing coincidences between the various detectors. The average intrinsic one-proton detection efficiency of the proton branch was determined to be 79(2)%, the error being purely statistical.

The opening angle of the beam line downstream from the target is around 80 mrad. Therefore, a correction for acceptance cuts along the beam line is needed. To determine the geometric acceptance of the experimental setup as a function of the relative energy of the ejectiles, a simulation package using the R3BROOT framework was used [34]. This package permits one to simulate fragment and proton tracks through the setup. A simple phase-space event generator was employed to produce fragment and proton breakup events. The geometric acceptance curve is presented in Fig. 9, showing a quite flat behavior up to 3 MeV, followed by a constant decline with increasing relative energy, mainly from increasing proton losses in the y direction in the ALADIN magnet.

D. Evaluation of coincident γ rays

The radiative-capture cross section $\sigma_{\gamma p}$ can be calculated from the CD one, σ_{CD}, only if the Coulomb-breakup reaction feeds directly the ^{26}Si ground state. Reactions passing through

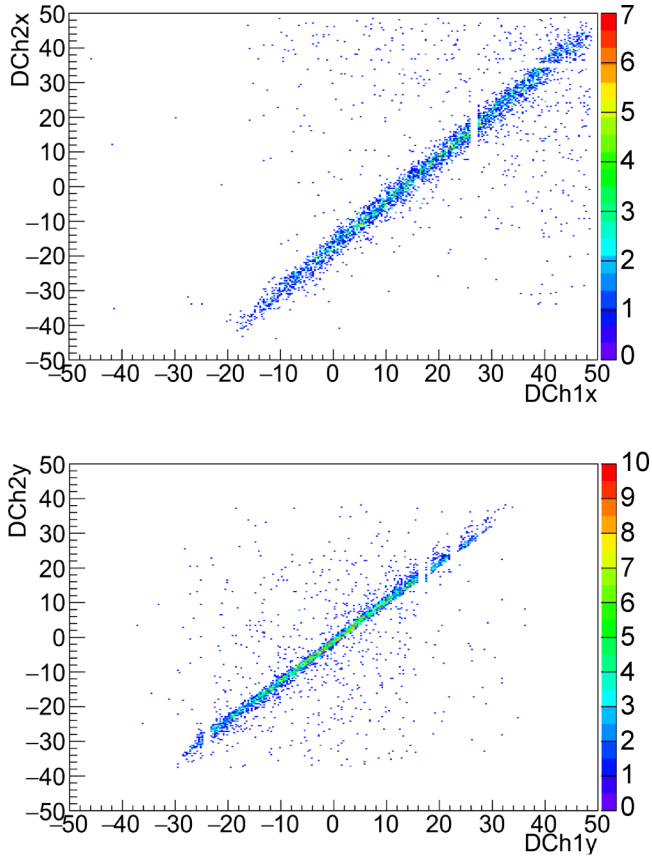

FIG. 8. Position correlations of tracked breakup protons on both DCH detectors; top panel, correlation of x positions; bottom panel, correlation of y positions. The empty spaces in the data originate from broken wires in the DCH, which was taken care of in the simulation.

excited states in ^{26}Si were detected by recording coincident de-excitation γ rays in the crystal-ball γ-ray detector, XB. Figure 10 shows the γ-ray sum spectrum up to 4 MeV measured in coincidence with ^{26}Si fragments and protons stemming from ^{27}P breakup in the $^{\text{nat}}$Pb target.

In Fig. 10, the experimental data are compared to the simulated response of XB. For this purpose, the simulation package R3BROOT [34] was employed, which contains the full geometrical information about the XB and allows one to fully simulate the photon interactions. The detected γ rays are mostly from atomic processes occurring in the relatively thick $^{\text{nat}}$Pb target. A peaklike structure at an energy of $\approx$0.6 MeV visible in the simulation as well as in the atomic-background distribution has no physical meaning. It results from the fact that two groups of XB crystals with different energy thresholds were used.

About 26% of the events shown in Fig. 10 originate from excited states in ^{26}Si. These γ rays contribute at energies above $\approx$ 1 MeV in Fig. 10. The following states have been considered: 1.797 MeV, 2.787 MeV, 3.337 MeV, 3.757 MeV, 3.842 MeV, 4.140 MeV, 4.446 MeV, 4.811 MeV [35].

The same simulation with R3BROOT was used to estimate the average efficiency of XB. The efficiency had to be averaged over all γ-ray energies because of the overlap of the γ lines.

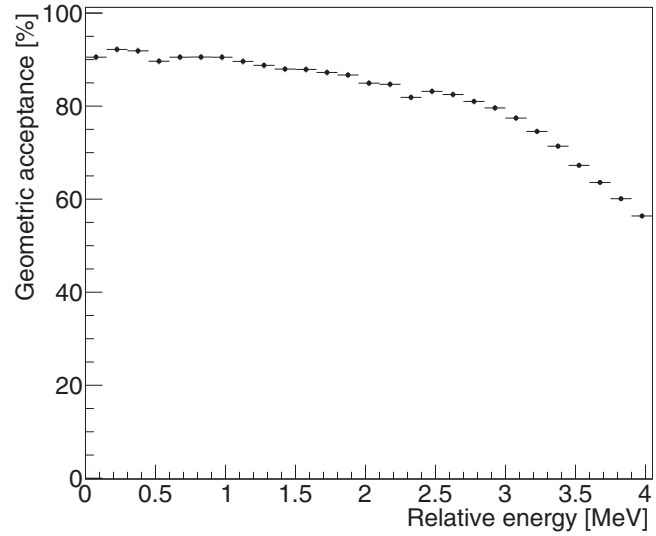

FIG. 9. Geometric acceptance of the experimental setup obtained by Monte Carlo simulations.

The efficiency was determined to be 83(5)%, the error being purely statistical.

E. Invariant-mass spectra

To extract spectroscopic information on ^{27}P, the invariant-mass method was used. Using the mass m_f of ^{26}Si and the proton mass m_p the proton-^{26}Si relative energy (equal to the ^{27}P excitation energy) is given by

$$E_r = \sqrt{m_f^2 + \gamma_f \gamma_p m_f m_p (1 - \beta_f \beta_p \cos\theta_{fp})} - (m_f + m_p), \tag{10}$$

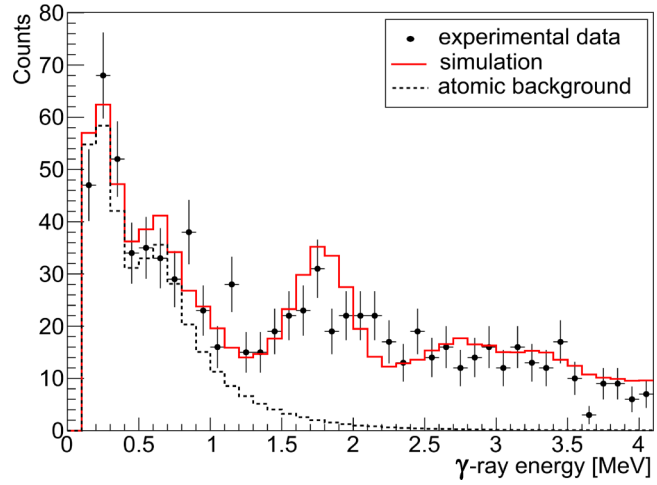

FIG. 10. Reconstructed γ-ray spectrum from the Crystal Ball for the reaction ^{27}P $\rightarrow$ ^{26}Si + proton in a $^{\text{nat}}$Pb target (black circles). The red histogram represents a simulation of the XB response, made with the R3BROOT package. The dashed histogram marks the atomic background (see text for details).

where $\gamma_{f,p}$ is the Lorentz factor for the heavy fragment and the proton, $\beta_{f,p}$ the velocities, and θ_{fp} the opening angle between the proton and ^{26}Si. Using this equation the relative-energy spectra for each target were obtained (Fig. 11). To select only the reaction to the ground state of ^{26}Si, relative-energy spectra for excited states were created using a one-dimensional gate in the XB γ-ray spectrum (Fig. 10) assuming that all events with γ-ray energies above 1.4 MeV were connected with excited states in ^{26}Si. Next these relative-energy spectra for excited states were corrected by the average XB efficiency and subtracted.

Figure 11 shows the relative-energy spectra resulting from direct feeding of the ground state.

In this figure, the solid circles with error bars represent the experimental data. The solid curve in the Pb-target spectrum (a) represents the result of a fit with five components: four resonances and a direct-capture component (dotted curves). The free parameters for the fit to the Pb-target spectrum are the heights and positions of the four peaks and the amplitude of the distribution for the direct-capture component. The widths of the peaks were fixed to the experimental resolutions, under the assumption that their natural widths are much smaller. For the direct-capture component the theoretical prediction of the shape was used (Sec. II D). For the carbon-target (b) and the empty-target spectrum (c) the free parameters were only the heights of the peaks and the amplitude of the direct-capture component. The positions and widths of the peaks were taken from fitting the Pb spectrum because of the much better statistics. The peak energies for the Pb-target spectrum were also used to slightly rescale the energy axes of the carbon- and empty-target spectra.

To disentangle nuclear contributions from the electromagnetic excitations induced in the ^{nat}Pb target, the data taken with ^{12}C target were scaled and subtracted from the Pb-target data set (see Ref. [36]). The nuclear contribution turns out to be relatively small (around 14%). To treat background contributions from layers of matter other than the target properly, data taken with an empty target frame have also been subtracted from the data set. Because of very poor statistics in particular in the empty-target run, the fitted curves of the

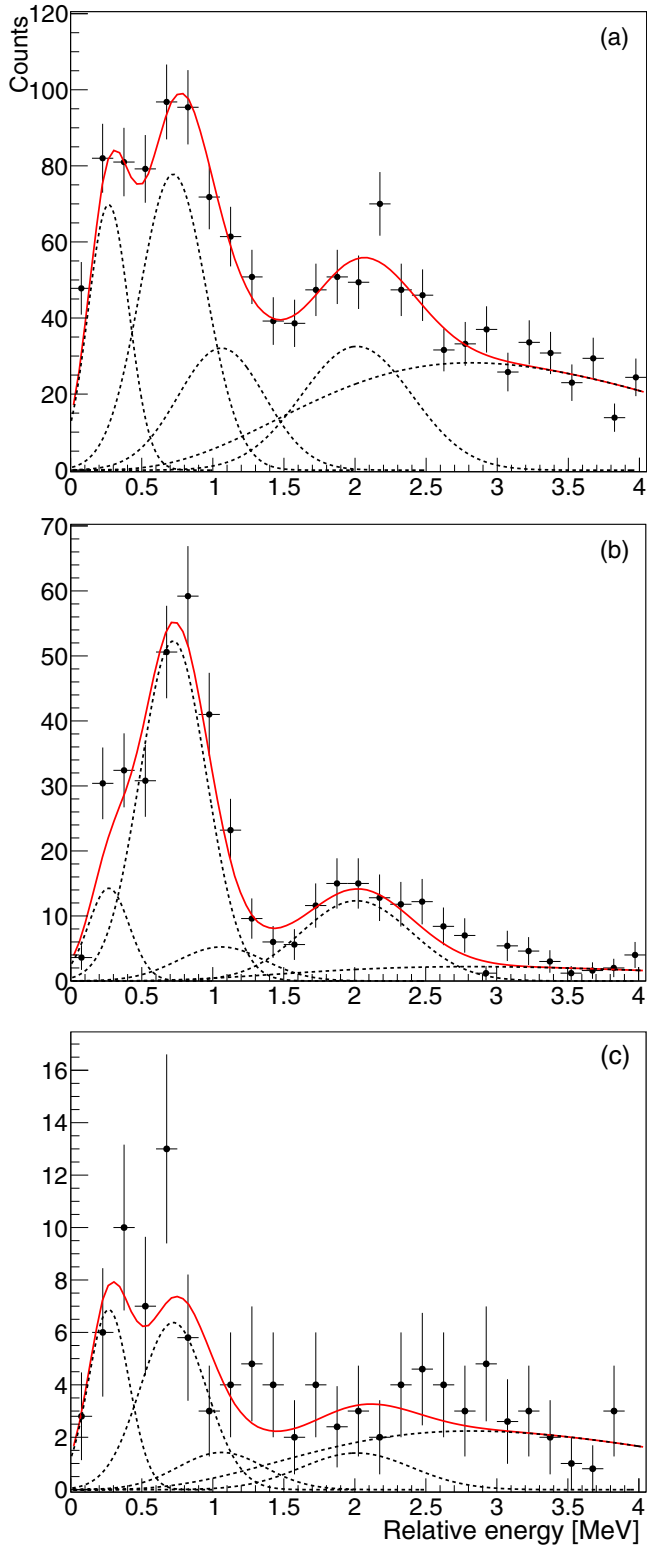

FIG. 11. Invariant-mass spectra for ^{27}P impinging on (a) a ^{nat}Pb target, (b) a ^{12}C target, and (c) an empty target frame.

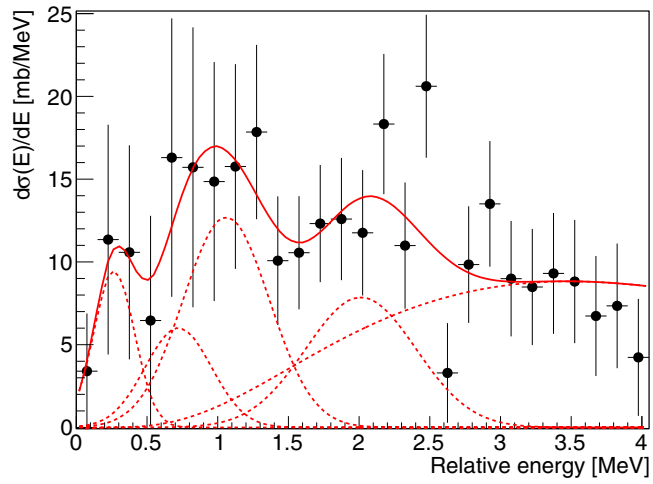

FIG. 12. Invariant-mass spectrum for the CD of ^{27}P feeding directly the ground state of ^{26}Si. Nuclear and empty-target contributions have been subtracted (see text).

TABLE IV. Relative energies and excitation energies of low-lying resonances in ^{27}P. Excitation energies from the present work were calculated using the proton binding energy of 870(26) keV given by Ref. [9].

Present		Jung *et al.* [12]	Togano *et al.* [8]	Gade *et al.* [11]	Caggiano *et al.* [4]
E_r (MeV)	$E_{\rm exc}$ (MeV)	$E_{\rm exc}$ (MeV)	$E_{\rm exc}$ (MeV)	$E_{\rm exc}$ (MeV)	$E_{\rm exc}$ (MeV)
0.267(20)	1.137(33)		1.176(32)	1.120(8)	1.199(19)
0.722(56)	1.592(62)		1.666(42)		1.631(19)
1.060(170)	1.930(172)		2.23(10)		
2.012(76)	2.882(80)	2.880(29)	3.06(9)		

carbon- and empty-target spectra [full lines in Figs. 11(b) and 11(c)] have been used for the subtraction instead of the experimental histograms.

Figure 12 shows the background-subtracted relative-energy-differential spectrum for ^{27}P for pure Coulomb dissociation.

The solid circles represent the experimental data. The solid curve represents the result of a fit with five components. The fitting procedure is the same as the one described above. The free parameters for the fit were the heights of the peaks and the amplitude of the direct-capture component. The positions of the peaks were taken from the fitting of the Pb-target spectrum, where peaks 1, 2, and 4 are well defined; the widths of the peaks were fixed to the experimental resolutions. The four resonances and a direct-capture component can be distinguished. Table IV lists the results of the relative energies and excitation energies for the states observed in this study together with previously reported results [4,8,11,12]. The present results are in agreement with previous data within the range of uncertainties.

In Table V the CD cross sections $\sigma_{\rm CD}$ populating the resonances in ^{27}P are shown. The given uncertainties are purely statistical; the common systematic uncertainty is 6%. The systematic error includes the uncertainties of the detector efficiencies and the target thicknesses.

The CD cross section up to 4 MeV of relative energy of the direct-breakup component, which corresponds to the inverse process of the direct proton capture in the ^{26}Si(p,γ)^{27}P reaction, was calculated to be 19.2(2.3) mb.

F. Monte Carlo simulation

A Monte Carlo simulation was made to compare the theoretical predictions to the experimental data. A theoretical input file (see Sec. II D) containing 500 000 "events" was sent through the experimental setup (Fig. 4) using the R3BROOT framework [34]. To simulate the penetration of the particles through the different materials, GEANT3 and GEANT4 data bases were utilized. The outgoing simulated data were tracked with the experimental tracking algorithm. In this way, the theoretical "events" were analyzed exactly in the same way as the experimental ones. When comparing the widths of the peaks fitted to the simulated data to those of the experimental resonance peaks (see Fig. 12), we found that the peaks in the experiment were broader than predicted by the detector resolution and the straggling contribution. We attribute this to uncertainties in the detector positions in combination with the tracking algorithm. Additional Gaussian broadening was therefore added in the simulation to match the widths of the experimental peaks.

Figure 13 shows the comparison between the experimental data (from Fig. 12, solid circles with error bars) and the theoretical predictions (histogram). The full curves denote peaks fitted to the histogram, where the peak positions were taken from the experiment. The red dashed curves and the long-dashed sum curve represent the experimental results taken from Fig. 12. Note that the strength of the fourth resonance at $E_r = 2.01$ MeV ($E_{\rm exc} = 2.882$ MeV) was scaled down by a factor of 0.425 to match the experimental cross section.

V. DISCUSSION

A comparison of the final data from the present experiment to those from the other study of the ^{27}P Coulomb breakup by Togano *et al.* [8] shows that the statistics of our results is comparable to or even better than that of Ref. [8]. This can be seen by comparing Fig. 11(a) with the equivalent Fig. 3 in Ref. [8], both taken with a Pb target and shown with identical bin width. Three peaks at $E_r \approx 0.27, 0.72$, and 2.01 MeV can be clearly identified in both spectra.

Our evidence for the peak at $E_r \approx 1$ MeV is less convincing; its existence is, however, suggested by both the width of

TABLE V. CD cross sections $\sigma_{\rm CD}$ through the four lowest-lying resonances in ^{27}P.

E_r (MeV)	$E_{\rm exc}$ (MeV)	Transition	Multipolarity	$\sigma_{\rm CD-exp}$ (mb)	$\sigma_{\rm CD-theo}$ (mb)
0.267(20)	1.137	$\frac{1}{2}^+_{gs} \rightarrow \frac{3}{2}^+_1$	$M1+E2$	3.3(1.7)	3.8
0.722(56)	1.592	$\frac{1}{2}^+_{gs} \rightarrow \frac{5}{2}^+_1$	$E2$	3.5(3.1)	5.6
1.060(170)	1.930	$\frac{1}{2}^+_{gs} \rightarrow \frac{5}{2}^+_2$	$E2$	9.7(3.0)	6.0
2.012(76)	2.882	$\frac{1}{2}^+_{gs} \rightarrow \frac{3}{2}^-$	$E1$	7.6(1.9)	17.9*

*In the simulation normalized to the experimental data.

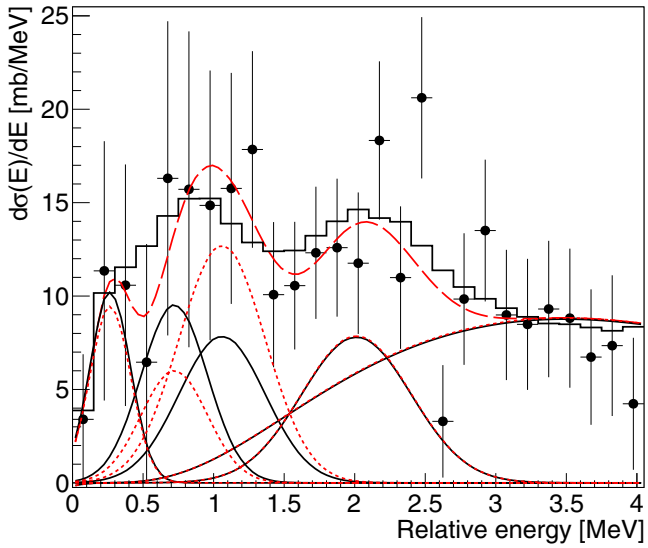

FIG. 13. Comparison between the experimental invariant-mass spectrum (solid circles with error bars) and a simulated one using the theoretical predictions (histogram). The solid curves represent Gaussian peaks fitted to the histogram. The red dashed curves and their sum curve (long dashed) result from fits to the experimental data. Note that in the simulation the strength of the fourth resonance at $E_r = 2.01$ MeV was scaled down to match the experimental cross section.

the second peak in Fig. 11(a) and the levels found in the mirror nucleus, ^{27}Mg (see Fig. 1). We find this resonance at an energy of $E_r = 1.06(17)$ MeV compared to $E_r = 1.37(10)$ MeV reported in Ref. [8]. As expected, our spectrum shows a more pronounced nonresonant direct-capture component, which accounts for all of the counts recorded between 3 and 4 MeV of relative energy in Fig. 11(a). Note that the shape of this component was taken from the theoretical model described in Sec. II C; only the amplitude was scaled to the data.

The Gaussian peak fits to the data in Fig. 11(a) define to a large extent the resonance energies listed in column 2 of Table IV. We note in particular the good agreement of our energy value of the first resonance with the precise value measured by Gade *et al.* [11] by γ-ray spectroscopy. The fourth resonance that we locate at 2.882(80) MeV deserves a special comment. In the proton-elastic-scattering experiment of Jung *et al.*, a $7/2^+$ resonance was found at 2.880(29) MeV [12]. Such a resonance cannot be reached by CD from the $1/2^+$ g.s. of ^{27}P. We have therefore discussed this aspect with the principal author of Ref. [12], H. S. Jung, leading to a re-evaluation of the R matrix fits to the elastic-scattering cross sections. Jung observed that the quality of the fits deteriorated only insignificantly if a $3/2^-$ assignment was chosen for the 2.88-MeV resonance instead of $7/2^+$, contrary to other choices ($3/2^+$, $5/2^+$), which lead to a much larger χ^2 value. In Ref. [12], a negative-parity resonance was not considered because none was known in the mirror nucleus ^{27}Mg at this energy. Negative-parity states do not show up in shell-model calculations, neither in Ref. [12] nor in Ref. [8], because they were performed in the sd-shell-model space, which yield only positive-parity states. Based on the discussion of the new R-matrix fits by Jung, we tend to equate our fourth resonance peak with the 2.88-MeV $3/2^-$ level excited in the proton-elastic-scattering experiment of Ref. [12] at exactly the same energy. We consider this as the first experimental evidence for a low-lying negative-parity intruder state in ^{27}P.

The comparatively good statistics presented in Fig. 11(a) deteriorates considerably when we correct for reactions from nuclear interactions, measured with a ^{12}C target [see Fig. 11(b)], as well as for reactions in layers of matter other than the target [see Fig. 11(c)]. In particular the latter experiment suffers from insufficient statistics. The resulting invariant-mass spectrum for pure Coulomb interactions leading to the ^{26}Si (g.s.) (Fig. 12) is therefore characterized by large error bars and no pronounced peak structure, which is reflected in the large errors of the experimental CD cross sections, listed in column 5 of Table V. For the first $3/2^+$ resonance the corresponding theoretical value (column 6 of Table V) is in very good agreement. For the following two unresolved $5/2^+$ resonances, the theory predicts a smaller value for the second and a larger one for the third resonance, while in experiment the cross sections behave in the opposite way. However, the sum of both experimental and theoretical cross sections agree well again. A $3/2^-$ assignment to the fourth resonance leads to a strong $E1$ transition and a correspondingly large theoretical CD cross section of 17.9 mb, clearly much larger than the experimental cross section of only 7.6(1.9) mb. A $3/2^+(5/2^+)$ assignment would lead to a theoretical cross section of 5.2(7.8) mb, but both assignments are in conflict with the poor R-matrix fits of Ref. [12] mentioned above. We postulate therefore a reduction in strength by a factor of 0.425 for the fourth resonance and keep the $3/2^-$ assignment.

VI. THERMONUCLEAR REACTION RATE

The role played by the ^{26}Si(p,γ)^{27}P reaction in a thermonuclear reaction network depends on the total reaction rate,

$$N_A\langle\sigma v\rangle^{\rm tot} = \sum_i N_A\langle\sigma v\rangle_i^{\rm res} + N_A\langle\sigma v\rangle^{\rm dc}, \qquad (11)$$

which is the sum of all rates of narrow resonances plus the direct-capture component. For a narrow resonance, the thermonuclear reaction rate can be approximated via [37]

$$N_A\langle\sigma v\rangle_i^{\rm res} = 1.54\times10^{11}(AT_9)^{-3/2}(\omega\gamma)e^{-11.605E_r/T_9}, \qquad (12)$$

with A being the reduced massed of the (^{26}Si$+p$) system and T_9 the temperature in GK; $\omega\gamma$ denotes the resonance strength, and E_r the resonance energy in keV. The resonance strength $\omega\gamma$ was defined in Eq. (5). We emphasize that for the dominant first $3/2^+_1$ resonance our measurement is sensitive only to the small $E2$ component, so that the resonance strength is largely defined by the $M1$ component calculated theoretically in Sec. II C. The resonance energy of this state is most precisely given by the γ-ray energy of $E_\gamma = 1120(8)$ keV measured in Ref. [11] and the Q value of 870(26) keV (Ref. [9]) yielding $E_r = 250(27)$ keV, in good agreement with our value of 267(20) keV and the one used in the compilation of Iliadis *et al.* [5] of 259(28) keV. The partial proton and γ widths of the first resonance in Ref. [5] have been adapted to match the mirror nucleus or have been newly calculated. Generally, they

are in reasonable agreement with our extracted partial widths within a factor of 4. These and all other resonance parameters needed to calculate the reaction rates are listed in Table IV.

The second term in Eq. (11), the direct-capture reaction rate, is directly related to the astrophysical S factor, $S(E)$ [Eq. (6)]. As can be seen from Fig. 2 the S factor is a relatively slowly varying function of energy outside the narrow resonances. In this case, the direct-capture component can be calculated using an *effective S-factor* $S_{\rm eff}$ derived in [37] with

$$S_{\rm eff} \approx S(0)\left(1 + 0.1\frac{T_9^{1/3}}{\left(Z_1^2 Z_2^2 A\right)^{1/3}}\right), \qquad (13)$$

with $S(0)$ being the S factor at $E = 0$, and $Z_{1,2}$ the corresponding charges of the interacting particles. With this approximation, the direct-capture reaction rate is then given by the expression,

$$N_A\langle\sigma v\rangle^{\rm dc} = 7.83 \times 10^9 \left(\frac{Z_1 Z_2}{A}\right)^{1/3} T_9^{-2/3} \times S(0) \times \exp\left(-4.25 T_9^{-1/3}\left(Z_1^2 Z_2^2 A\right)^{1/3}\right).$$

As mentioned above, the high-energy part of our relative-energy spectrum, Fig. 12, yields $S(0) = 35.9$ keV b, very close to the value of $S(0) = 36.3$ keV b calculated in Ref. [22], but only two-thirds of the value of 54.5 keV b used in Ref. [5]. The discrepancy is much larger, however, with the value of $S(0) = 87(11)$ keV b extracted from a measurement of the asymptotic normalization coefficient for the mirror nucleus ^{27}Mg [21].

Using the equations given above the thermonuclear reaction rates can be calculated, they are shown in Table VI and Fig. 14. Figure 14(a) shows the single resonance contributions and the direct-capture component of the total reaction rate in the temperature window $0.01 < T_9 < 2$ GK. Clearly, proton capture into the first $3/2^+$ resonance dominates the reaction rate under typical nova conditions. The direct-capture component is negligible when the temperature exceeds 0.06 GK. All higher-lying resonances contribute only a minor fraction to the total reaction rate below 2 GK.

In Fig. 14(b) the total reaction rates of this work are shown by the $\pm 1\sigma$-uncertainty band, in comparison with similar data from the compilation by Iliadis *et al.* [5] and the work of Togano *et al.* [8]. We display in Fig. 14(c) the same data as ratios normalized to our results. The main contribution to the overall uncertainty in our data stems from the errors of the resonance energies, which enter exponentially into the total rate. Our suggested rate is in excellent agreement with the evaluated rate from the Iliadis *et al.* [5] compilation. The agreement is not so good with the data published by Togano *et al.* [8]. Here, the two rates differ considerably in the important temperature range. We believe that this is mainly because of a discrepancy in the extracted excitation energy and the spectroscopic strength of the first resonance. The excitation energy extracted by Togano *et al.* of 1176(32) keV is in agreement, within uncertainty, with our value of 1137(33) keV, however, it is not in agreement with the measurement by Gade *et al.* of 1120(8) keV. In addition, the resonance strength of Togano *et al.* for the first resonance is a factor of 3 larger than our measurement suggests, which is because of a different model calculation of the $M1$ component (see Table II). This small deviation in the resonance strength is enhanced by the difference in the excitation energy. At temperatures above 0.3 GK all three reaction rates shown in Figs. 14(b) and 14(c) are in good agreement.

TABLE VI. The thermonuclear reaction rate for ^{26}Si(p,γ)^{27}P from this work. The units are cm^{3}mol^{-1}s^{-1}. The 1σ uncertainties are given.

T_9 [GK]	$N_A\langle\sigma v\rangle^{\rm total}$	$N_A\langle\sigma v\rangle^{\rm low}$	$N_A\langle\sigma v\rangle^{\rm high}$
0.01	1.10×10^{-39}	5.52×10^{-40}	2.21×10^{-39}
0.02	9.49×10^{-30}	4.74×10^{-30}	1.90×10^{-29}
0.03	6.15×10^{-25}	3.08×10^{-25}	1.23×10^{-24}
0.04	6.61×10^{-22}	3.31×10^{-22}	1.32×10^{-21}
0.05	9.43×10^{-20}	4.71×10^{-20}	2.09×10^{-19}
0.06	4.40×10^{-18}	2.06×10^{-18}	1.11×10^{-16}
0.07	4.39×10^{-16}	4.32×10^{-17}	4.34×10^{-14}
0.08	7.44×10^{-14}	1.03×10^{-15}	3.91×10^{-12}
0.09	4.56×10^{-12}	6.58×10^{-14}	1.27×10^{-10}
0.10	1.21×10^{-10}	2.76×10^{-12}	2.02×10^{-09}
0.15	2.02×10^{-06}	2.07×10^{-07}	7.17×10^{-06}
0.20	2.30×10^{-04}	5.03×10^{-05}	3.76×10^{-04}
0.30	2.19×10^{-02}	1.02×10^{-02}	2.26×10^{-02}
0.40	1.88×10^{-01}	9.63×10^{-02}	1.89×10^{-01}
0.50	6.33×10^{-01}	2.57×10^{-01}	6.65×10^{-01}
0.60	$1.35 \times 10^{+00}$	4.71×10^{-01}	$1.51 \times 10^{+00}$
0.70	$2.25 \times 10^{+00}$	7.01×10^{-01}	$2.65 \times 10^{+00}$
0.80	$3.20 \times 10^{+00}$	9.19×10^{-01}	$3.98 \times 10^{+00}$
0.90	$4.13 \times 10^{+00}$	$1.11 \times 10^{+00}$	$5.39 \times 10^{+00}$
1.00	$4.99 \times 10^{+00}$	$1.28 \times 10^{+00}$	$6.80 \times 10^{+00}$
1.50	$8.02 \times 10^{+00}$	$1.89 \times 10^{+00}$	$1.28 \times 10^{+01}$
2.00	$1.05 \times 10^{+01}$	$2.85 \times 10^{+00}$	$1.84 \times 10^{+01}$
2.50	$1.56 \times 10^{+01}$	$5.60 \times 10^{+00}$	$2.87 \times 10^{+01}$
3.00	$2.68 \times 10^{+01}$	$1.20 \times 10^{+01}$	$5.00 \times 10^{+01}$
4.00	$8.03 \times 10^{+01}$	$4.25 \times 10^{+01}$	$1.49 \times 10^{+02}$
5.00	$1.90 \times 10^{+02}$	$1.04 \times 10^{+02}$	$3.54 \times 10^{+02}$
6.00	$3.70 \times 10^{+02}$	$2.03 \times 10^{+02}$	$6.95 \times 10^{+02}$
7.00	$6.28 \times 10^{+02}$	$3.40 \times 10^{+02}$	$1.19 \times 10^{+03}$
8.00	$9.70 \times 10^{+02}$	$5.20 \times 10^{+02}$	$1.86 \times 10^{+03}$
9.00	$1.40 \times 10^{+03}$	$7.43 \times 10^{+02}$	$2.71 \times 10^{+03}$
10.00	$1.93 \times 10^{+03}$	$1.01 \times 10^{+03}$	$3.75 \times 10^{+03}$

Iliadis *et al.* [38] have investigated the production of ^{26}Al in heavy stars based on the reaction rate compilation [5] contained in STARLIB [7]. The good agreement between our reaction rate and that of the compilation gives additional confidence in the conclusions of Ref. [38]: It turns out that all relevant ^{26}Al production mechanisms proceed somewhat close to β stability and are thus largely independent of the ^{26}Si(p,γ)^{27}P reaction rates. This is true irrespective of whether thermal equilibrium between the ground and isomeric states of ^{26}Al is assumed or not [38].

VII. SUMMARY

In summary we have extracted the low-lying level scheme and the corresponding resonance strengths of ^{27}P using Coulomb breakup of ^{27}P at 500 MeV/nucleon with

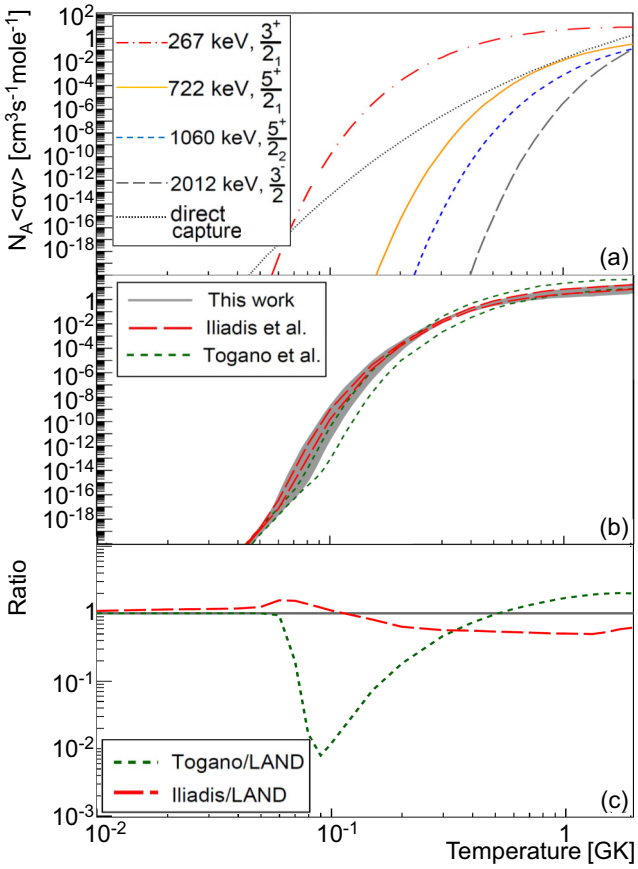

FIG. 14. Calculated thermonuclear reaction rates (a) The single-resonance and direct-capture contributions from this work; (b) the $\pm 1\sigma$-uncertainty bands of the total reaction rates from this work (shaded band) in comparison with those from Togano *et al.* ([8], short dashed), and Iliadis *et al.* ([5], long dashed); (c) ratios of the Togano *et al.* [8] and the Iliadis *et al.* [5] reaction rates divided by those of the present work.

the ALADIN-LAND setup of the GSI Helmholtzzentrum für Schwerionenforschung in Darmstadt, Germany. For the energies of the two lowest resonances, we find good agreement with previously published data. We locate the third resonance 0.3 MeV lower than a similar CD study performed at 54.2 *A* MeV [8]. We find experimental evidence for a negative-parity $3/2^-$ intruder state at an excitation energy of 2882(80) keV, in agreement with re-evaluated results from Ref. [12]. Detailed theoretical calculations of the CD cross sections with the CDXS+ code, based on a simple potential model, yield predictions that are in overall good agreement with our data. Based on our data we derive a zero-energy *S* factor of $S(0) = 35.9$ keV b, which is in very good agreement with a previous shell-model calculation by Herndl *et al.* [22]. It disagrees, however, by a factor of 2.5 with $S(0) = 87(11)$ keV b extracted from a measurement of the asymptotic normalization coefficient for the mirror nucleus ^{27}Mg [21].

Astrophysically, we calculate thermonuclear reaction rates which agree well within uncertainties with the currently suggested rates given in the REACLIB [6] and STARLIB [7] compilations. Under nova conditions the rate is mainly determined by capture into the first $3/2^+$ resonance. Contrary to naive expectations, however, the ^{26}Si(p,γ)^{27}P reaction is irrelevant for the question how much ^{26}Al is produced in the galaxy.

ACKNOWLEDGMENTS

The authors wish to thank Hyo Soon Jung for helpful discussions and her re-analysis of the proton-elastic-scattering experiment. This project was supported by BMBF, EU(EURONS), EMMI, GSI Darmstadt, FIAS, NAVI, GSI-TU Darmstadt cooperation, and HIC for FAIR. S.T. was supported by the Helmholtz Association (HGF) through the Nuclear Astrophysics Virtual Institute (VH-VI-417). C.L. acknowledges support from JINA-CEE under Grants No. PHY-1430152 and No. PHY-0822648 of the National Science Foundation. S.B.N. and the University of Santiago de Compostela group acknowledge support from the Spanish Ministerio de Educacion, under Grants No. FPU-AP2006-01474, No. FPA2012-39404-C02-01, and No. FPA2013-47831-C2-1 and from Xunta de Galicia under Grant No. GRC2013-11.

[1] R. Diehl *et al.*, Astron. Astrophys. **298**, 445 (1995).
[2] R. Diehl *et al.*, Astron. Astrophys. **449**, 1025 (2006).
[3] N. Prantzos and R. Diehl, Phys. Rep. **267**, 1 (1996).
[4] J. A. Caggiano, D. Bazin, W. Benenson, B. Davids, R. Ibbotson, H. Scheit, B. M. Sherrill, M. Steiner, J. Yurkon, A. F. Zeller, B. Blank, M. Chartier, J. Greene, J. A. Nolen, Jr., A. H. Wuosmaa, M. Bhattacharya, A. Garcia, and M. Wiescher, Phys. Rev. C **64**, 025802 (2001).
[5] C. Iliadis *et al.*, Nucl. Phys. A **841**, 31 (2010).
[6] R. Cyburt *et al.*, Astrophys. J. Suppl. **189**, 240 (2010).
[7] A. L. Sallaska *et al.*, Astrophys. J. Suppl. **207**, 18 (2013).
[8] Y. Togano, T. Gomi, T. Motobayashi, Y. Ando, N. Aoi, H. Baba, K. Demichi, Z. Elekes, N. Fukuda, Z. Fulop, U. Futakami, H. Hasegawa, Y. Higurashi, K. Ieki, N. Imai, M. Ishihara, K. Ishikawa, N. Iwasa, H. Iwasaki, S. Kanno, Y. Kondo, T. Kubo, S. Kubono, M. Kunibu, K. Kurita, Y. U. Matsuyama, S. Michimasa, T. Minemura, M. Miura, H. Murakami, T. Nakamura, M. Notani, S. Ota, A. Saito, H. Sakurai, M. Serata, S. Shimoura, T. Sugimoto, E. Takeshita, S. Takeuchi, K. Ue, K. Yamada, Y. Yanagisawa, K. Yoneda, and A. Yoshida, Phys. Rev. C **84**, 035808 (2011).
[9] G. Audi, F. G. Kondev, M. Wang, B. Pfeiffer, X. Sun, J. Blachot, and M. MacCormick, Chinese Phys. C **36**, 1157 (2012).
[10] M. S. Basunia, Nucl. Data Sheets **112**, 1875 (2011).
[11] A. Gade, P. Adrich, D. Bazin, M. D. Bowen, B. A. Brown, C. M. Campbell, J. M. Cook, T. Glasmacher, P. G. Hansen, K. Hosier, S. McDaniel, D. McGlinchery, A. Obertelli, K. Siwek, L. A. Riley, J. A. Tostevin, and D. Weisshaar, Phys. Rev. C **77**, 044306 (2008).
[12] H. S. Jung, C. S. Lee, Y. K. Kwon, J. Y. Moon, J. H. Lee, C. C. Yun, S. Kubono, H. Yamaguchi, T. Hashimoto, D. Kahl, S. Hayakawa, S. Choi, M. J. Kim, Y. H. Kim, Y. K. Kim, J. S.

Park, E. J. Kim, C. B. Moon, T. Teranishi, Y. Wakabayashi, N. Iwasa, T. Yamada, Y. Togano, S. Kato, S. Cherubini, and G. G. Rapisarda, Phys. Rev. C **85**, 045802 (2012).
[13] S. Typel, Computer program FORTRAN`cdxsp.f`, Version 6.57 (unpublished).
[14] S. Typel and B. A. Brown, Phys. Rev. C **67**, 034313 (2003).
[15] B. A. Brown, Phys. Rev. C **58**, 220 (1998).
[16] R. B. Firestone, Nucl. Data Sheets **110**, 1691 (2009).
[17] M. S. Basunia, Nucl. Data Sheets **113**, 909 (2012).
[18] A. Bohr and B. R. Mottelson, *Nuclear Structure*, Vol. II (Benjamin, Reading, 1975).
[19] D. Costa and F. A. Beck, Nucl. Phys. A **181**, 132 (1972).
[20] M. A. de Voigt, P. W. M. Glaudemans, I. de Boer, and H. Wildenthal, Nucl. Phys. A **186**, 365 (1972).
[21] B. Guo, Z. H. Li, X. X. Bai, W. P. Liu, N. C. Shu, and Y. S. Chen, Phys. Rev. C **73**, 048801 (2006).
[22] H. Herndl, J. Görres, M. Wiescher, B. A. Brown, and L. Van Wormer, Phys. Rev. C **52**, 1078 (1995).
[23] A. Winther and K. Alder, Nucl. Phys. A **319**, 518 (1979).
[24] C. Langer *et al.*, Phys. Rev. C **89**, 035806 (2014).
[25] H. Geissel *et al.*, Nucl. Instr. and Meth. B **70**, 286 (1992).
[26] J. Cub *et al.*, Nucl. Instr. and Meth. A **402**, 67 (1998).
[27] K. Mahata *et al.*, Nucl. Instr. and Meth. A **608**, 331 (2009).
[28] http://web-docs.gsi.de/gsgweb/proj/cb_project.html.
[29] C. Scheidenberger and H. Geissel, Nucl. Instr. and Meth. B **135**, 25 (1998).
[30] http://web-docs.gsi.de/-pl2X-sim-weick/atima/.
[31] C. Langer, Ph.D. thesis, Johann-Wolfgang-Goethe University, Frankfurt, 2012.
[32] S. Beceiro Novo, Ph.D. thesis, Universidade de Santiago de Compostela, 2011. This article comprises essential parts of this Ph.D. thesis.
[33] F. Wamers, Ph.D. thesis, Technische Universität, Darmstadt, 2011.
[34] D. Bertini, J. Phys. Conf. Ser. **331**, 032036 (2011).
[35] http://www.nndc.bnl.gov/nudat2/chartNuc.jsp.
[36] K. Boretzky, A. Grunschloss, S. Ilievski, P. Adrich, T. Aumann, C. A. Bertulani, J. Cub, W. Dostal, B. Eberlein, T. W. Elze, H. Emling, M. Fallot, J. Holeczek, R. Holzmann, C. Kozhuharov, J. V. Kratz, R. Kulessa, Y. Leifels, A. Leistenschneider, E. Lubkiewicz, S. Mordechai, T. Ohtsuki, P. Reiter, H. Simon, K. Stelzer, J. Stroth, K. Summerer, A. Surowiec, E. Wajda, and W. Walus (LAND Collaboration), Phys. Rev. C **68**, 024317 (2003).
[37] W. A. Fowler, G. R. Caughlan, and B. A. Zimmerman, Annu. Rev. Astron. Astrophys. **5**, 525 (1967).
[38] C. Iliadis *et al.*, Astrophys. J. Suppl. **193**, 16 (2011).